

## Titan's vertical aerosol structure at the Huygens landing site: Constraints on particle size, density, charge, and refractive index

P. Lavvas\*, R.V. Yelle, C.A. Griffith

Lunar and Planetary Laboratory, University of Arizona, Tucson, USA

### ARTICLE INFO

#### Article history:

Received 1 February 2010

Revised 29 July 2010

Accepted 30 July 2010

Available online 11 August 2010

#### Keywords:

Titan

Atmospheres

### ABSTRACT

We present a one dimension simulation of Titan's aerosol distribution and compare our results with the haze optical properties retrieved by the DISR observations (Tomasko, M.G., Doose, L., Engel, S., Dafeo, L.E., West, R., Lemmon, M., Karkoschka, E., See, C. [2008]. *Planet. Space Sci.* 56, 669–707). We set the mass production of aerosols in the thermosphere to  $3 \times 10^{-14} \text{ g cm}^{-2} \text{ s}^{-1}$  and follow the evolution of the particles due to coagulation, sedimentation and atmospheric mixing. We use the observed aerosol phase functions at 100 km to constrain the particle's charge density to  $15 \text{ e}/\mu\text{m}$ . With this charge density, the microphysical model predictions for the number of monomers, and the particle size and density, are in good agreement with the DISR measurements. In addition, we derive a new refractive index for the aerosols based on the single scattering albedo inferred from DISR measurements. The imaginary index is larger than previous estimates based on laboratory analogs, with an increasing absorption toward the near-IR. Our simulation provides a good description of the particle properties above 80 km, but we find that condensation effects must be included in order to interpret aerosol characteristics at lower altitudes.

© 2010 Elsevier Inc. All rights reserved.

### 1. Introduction

The interaction of Titan's main atmospheric constituents with solar radiation creates a multitude of complex organic molecules. Further chemical reactions among these gaseous species produces the organic aerosols that extend from the surface to the lower thermosphere. The aerosol structure can be separated into a main haze layer located below 300 km and multiple detached layers above, the location and extent of which varies with latitude (Rages et al., 1983; Porco et al., 2005). The Cassini measurements have also revealed the presence of a well defined and symmetric, detached layer located at 520 km and aerosols have also been detected in the ionosphere ( $\sim 1000 \text{ km}$ ) as heavy negative ions (Coates et al., 2007).

Analyses of Voyager observations of the main haze layer suggests that these particles are aggregates of quasi-spherical monomers (West et al., 1983; West and Smith, 1991). This hypothesis explains the strongly forward scattering character of the haze relative to the scattering properties of spheres. The optically effective size of the particles is roughly a micrometer, while their optical properties imply that the material constituting the haze is strongly absorbing in the UV and Visible range (Rages et al., 1983). The inferred imaginary index of the aerosols between 0.2 and  $0.6 \mu\text{m}$  is

similar to that of some laboratory produced haze analogs (tholins) (Khare et al., 1984). A review of the pre-Cassini knowledge on the properties of Titan's haze can be found in McKay et al. (2001).

Comparison of Voyager and ground-based measurements with 1-D aerosol microphysics models has led to a better understanding of the processes responsible for the formation and evolution of the observed haze structures. Initial work by Toon et al. (1980) set the ground for the simulation of Titan's aerosols through microphysical models and pointed out the sensitivity of the results to the particle's charge and the atmospheric dynamics. Toon et al. (1992) used the observed geometric albedo to constrain the particle size, while McKay et al. (1989, 1991) analyzed Titan's vertical thermal structure in order to elucidate the role of the aerosols in heating the stratosphere by the absorption of solar radiation. Cabane et al. (1992, 1993) and Rannou et al. (1995, 1997) further improved the aerosol microphysical description with the inclusion of aggregate particle formation. Comparison of these models with high phase angle observations, implies that the aggregates in the main haze layer are made of monomers with a radius of 66 nm and that the fractal structure is characterized by a dimension of  $D_f = 2$ . The inclusion of aggregate particles in the simulations provides a better understanding of the observed aerosol properties but is not able to explain all features. An adjustment to the tholin refractive index by a multiplication factor is required in order to fit UV, Visible and IR observations (McKay et al., 1989; Toon et al., 1992). The fit was significantly improved with the use of aggregates relative to spheres, while a cut-off in the haze abundance below 100 km was necessary

\* Corresponding author. Fax: +1 520 621 4933.

E-mail address: [lavvas@lpl.arizona.edu](mailto:lavvas@lpl.arizona.edu) (P. Lavvas).

in order to match the observed minimum at 0.62  $\mu\text{m}$  in the geometric albedo (Rannou et al., 2003).

Significant effort also has been devoted to the inclusion of advection effects in the aerosol description. Models of 2 and 3 dimensions have been developed and demonstrated the impact of dynamics on the produced aerosol distribution (Rannou et al. (2004) and references therein). These models predict that the atmospheric circulation concentrates the particles in the polar regions, at latitudes higher than  $\pm 60^\circ$ . This variation in the latitudinal aerosol distribution produces the observed stratospheric temperature variation and causes the North–South albedo asymmetry and the polar hood. In addition, Rannou et al. (2003) showed that advection of the haze particles could produce the Voyager-detected detached haze layer at  $\sim 350$  km.

Cassini measurements provided further information on the aerosol properties and origin. By combining measurements from the UltraViolet Imaging Spectrometer (UVIS), the Imaging Science Subsystem (ISS) and the Huygens Atmospheric Structure Instrument (HASI), Lavvas et al. (2009) derived constraints for the particle size and flux in the detached haze layer at 520 km. They find that at this altitude, particles have a quasi-spherical shape with a  $\sim 40$  nm radius. In addition, the derived mass flux of  $2.7\text{--}4.6 \times 10^{-14}$  g  $\text{cm}^{-2} \text{s}^{-1}$ , is sufficient to generate the main haze layer, without the requirement of production in the lower atmosphere, although aerosol production in the stratosphere is still possible. Furthermore, the formation of the detached layer was found to correlate with the transition of the particle growth mode from spherical to aggregate. Combining these results with energy deposition arguments they concluded that a large production of aerosols occurs in Titan's thermosphere (Lavvas et al., 2009).

The measurements of the Descent Imager/Spectral Radiometer (DISR) on the Huygens probe, provide *in situ* information on the optical properties, size and density of the particles present in the main haze layer (Tomasko et al., 2008). The measurements have verified many of the conclusions from previous investigations regarding the particles' optical properties. The retrieved phase functions confirmed the fractal-aggregate nature of the particles, and the wavelength dependent measurements verified the absorbing nature of the particles in the visible region. The new measurements provide much tighter constraints for the particle size and density than we had before, but new features are also observed. The haze layer appears to extend all the way to the surface contrary to previous investigations that found a clearing of the aerosols towards the surface (Rannou et al. (2003) and references therein). Moreover, the altitude variation of the aerosol extinction profiles show the presence of three distinct altitude regions (region I above 80 km, region II between 80 and 30 km, and region III between 30 km and the surface), defined by both a change in the shape of the extinction profile and in the optical constants. Finally, the wavelength variation of the haze opacity is different from the dependence expected based on the refractive index of laboratory analogs (Khare et al., 1984).

Given the greatly improved constraints from DISR, we investigate here whether the haze characteristics observed are consistent with our understanding of aerosol formation and evolution. We do this through comparison of the inferred characteristics with predictions of a microphysical model. Since we have *in situ* observations only along the Huygens's path, we perform our calculations in one dimension but we further discuss the impact of dynamics on our results. Based on the conclusion that the aerosol production takes place in the upper atmosphere (Lavvas et al., 2009), the properties of aerosols in the stratosphere will be a result of the microphysical (coagulation and sedimentation) and atmospheric processes (mixing, condensation) defining the evolution of their size distribution and density from high to low altitudes. Thus, the DISR measurements can be used as a constraint for the contri-

bution of all these processes on the aerosol properties. In the current approach we attempt to simulate the aerosol profile without the inclusion of condensation effects in order to constrain the impact of the latter process. The results justify this approach for altitudes above 80 km, while for lower altitudes the inclusion of condensation appears to be mandatory for understanding the observed features. In the accompanying paper, we describe in detail how we include the condensation processes in the current model, and discuss the resulting implications for the optical properties of particulates in the lower atmosphere.

## 2. Model description

We base our work on the model developed by Lavvas et al. (2008a) and extended it in order to include the formation of aggregates. We adopt a discrete volume grid, which leads to an aerosol continuity equation of the form (Toon et al., 1992):

$$\frac{\partial n_p}{\partial t} = -\frac{1}{r^2} \frac{\partial(r^2 \Phi(v_p))}{\partial r} + \frac{1}{2} \sum_{i=1}^{p-1} K(u_i, v_p - u_i) n(u_i) n(v_p - u_i) - n_p \sum_{i=1}^{N_{\max}} K(u_i, v_k) n(u_i) + p(v_p) \delta_{p,1} \quad (1)$$

where  $p$  indicates the volume grid,  $n(v_p)$  and  $\Phi(v_p)$  are the number density and flux of volume  $v_p$  particles, respectively,  $r$  is the plane-to-centric distance and  $K$  is the coagulation kernel. The first sum in the right-hand side describes the production of size  $v_p$  particles from smaller particles, the second is the loss of size  $v_p$  particles by coagulation with other particles to form bigger particles,  $p(v_p)$  describes the local photochemical production of this size particles (only for the first bin particles, thus, the presence of the Kronecker  $\delta$  function) and  $N_{\max}$  is the number of volume bins considered in the calculations. There are 20 bins used with an expanding bin structure (the volume ratio of two adjacent bins is set to 3) covering the range between 3 nm to 3  $\mu\text{m}$ .

The flux of the particles depends on sedimentation and eddy mixing:

$$\Phi(v_p) = -V_s n(v_p) - K n_a \frac{\partial(n(v_p)/n_a)}{\partial r} \quad (2)$$

where  $V_s$  is the settling velocity,  $K$  the eddy mixing coefficient and  $n_a$  the atmospheric density. The following sections describe the calculation of coagulation and settling velocity for spheres and aggregates. These are similar to the methods used in previous models (Toon et al., 1980; Cabane et al., 1993; Rannou et al., 2003) with some improvements regarding the settling properties of the fractal aggregates. The particles are eventually deposited at the surface. We consider that each different size particle is lost at the surface with a velocity that is the maximum between the settling velocity of the particle right above the surface, and the downward velocity imposed by the atmospheric mixing. The flux of the particles is zero at the top boundary.

The above equations hold for both spherical particles and aggregates of monomers since they describe the volume (mass) transferred between different bins. The growth mode of the particles affects only the coagulation kernel and is controlled by the aerosol fractal dimension assumed at each altitude with the latter being treated as a model parameter. The transition between spherical to aggregate growth is simulated by changing the fractal dimension from 3 to 2, with the two limiting cases interpolated with a hyperbolic tangent function over the altitude range of the transition. The location and width of the transition region were retrieved from the analysis of the detached haze layer (Lavvas et al., 2009) and are further discussed below. The size of the monomer particles composing the aggregates is calculated as the volume average

radius of the particles at the altitude corresponding to the midpoint of the fractal dimension transition. The number of monomers within each aggregate is then calculated based on the ratio of the volume of each bin to the volume of a monomer.

We assume the particles grow as spheres above the detached haze layer and as aggregates below. The mechanism that leads to this behavior is not clear and depends on the physical properties of the particles. Assuming the particles to be solid, spherical growth is possible only inside the production region where the large number of fresh particles leads to a homogeneous growth (S. Lebonnois, P. Rannou, private communication). This suggests that the transition must be near the bottom of the production region. In addition, there is also the possibility of a continuous chemical growth from the gas phase. It is a common assumption in microphysical models that the chemical processes producing the particles from the background gas, cease to be important once the particles reach a size of a few nanometer, beyond which coagulation takes over. This is a valid assumption if the production region is narrow and particles readily move out of it. But if the surface chemical growth of the particles proceeds over a wide altitude range with a significant rate, concurrently with their coagulation, the size and shape of the particles will be affected by this process as much as from coagulation. Monte-Carlo simulations combining both chemical (surface) growth and coagulation suggest that while the latter leads to an aggregate structure, the former acts in an opposite way, tending to make the particles more spherical (Balthasar and Frenklach, 2005; Morgan et al., 2007). Although these simulations were performed for laminar flame conditions they emphasize on the importance of chemical growth taking place along with coagulation.

### 2.1. Spheres

The coagulation of particles depends mainly on their size and the atmospheric conditions. For two spherical particles with radii  $r$  and  $s$ , the coagulation kernel can be written as (Pruppacher and Klett, 1978):

$$K_B(r, s) = 4\pi(D_r + D_s)(r + s)\beta \quad (3)$$

where

$$\frac{1}{\beta} = \frac{r + s}{r + s + \sqrt{\delta_r^2 + \delta_s^2}} + \frac{4(D_r + D_s)}{(r + s)\sqrt{\bar{V}_r^2 + \bar{V}_s^2}} \quad (4)$$

with

$$\delta_r = \frac{(2r + \lambda_r)^3 - (4r^2 + \lambda_r^2)^{3/2}}{6r\lambda_r} - 2r \quad (5)$$

is an interpolation formula (Fuch, 1964) that connects the high pressure continuum regime (Brownian limit) with the free-molecular (ballistic) regime. In the above,  $\bar{V}_r$  is the particle's thermal velocity,  $\lambda_r$  is the particle's mean free path and  $D_r$  the particle diffusivity. These parameters can be calculated from:

$$\bar{V}_r = \sqrt{\frac{8k_B T}{\pi M_r}}, \quad \lambda_r = \frac{8D_r}{\pi \bar{V}_r}, \quad D_r = \frac{k_B T f_{slip}}{6\pi \eta r} \quad (6)$$

with  $k_B$  Boltzman's constant,  $T$  and  $\eta_a$  the atmospheric temperature and dynamic viscosity,  $\bar{M}_r$  the particle mass and  $f_{slip}$  the Cunningham slip-flow correction term:

$$f_{slip} = 1 + 1.257K_n + 0.4K_n \exp(-1.1/K_n) \quad (7)$$

which is also an interpolation formula between the continuum ( $K_n < 1$ ) and free-molecular regime ( $K_n > 1$ ) based on the Knudsen number,  $K_n = \lambda_a/r$ , with  $\lambda_a$  the atmospheric mean free path. The settling velocity of spherical particles is given by:

$$V_s = \frac{2\rho g r^2}{9\eta} f_{slip} \quad (8)$$

which applies in both high and low pressure limits.

### 2.2. Fractals

The fractal characterization of an aggregate refers to a scaling law between the number of monomers composing it,  $N_p$ , and the characteristic size of the aggregate:

$$N_p \sim R_f^{D_f} \quad \text{or} \quad N_p = A \left( \frac{R_f}{r_m} \right)^{D_f} \quad (9)$$

with  $D_f$  the dimension of the fractal aggregate and  $r_m$  the monomer radius. The proportionality constant  $A$  depends on the way the radius  $R_f$  is defined and the processes that affect the aggregate formation, with typical values between 0.95 and 1.43 (see Friedlander (2000) and references therein). The characterization of an assembly of particles as fractals of a specific dimension corresponds to a statistical average of the whole population, while the variation of the dimension describes the variation of the aggregate structure from compact,  $D_f = 3$ , to linear (chain-like),  $D_f = 1$ .

The coagulation kernel for aggregate structures can be calculated based on the spherical equivalent formulas for the radius of the fractal particle (Cabane et al., 1993). For the limiting cases of the free-molecular and continuum regimes the coagulation kernels for aggregates of dimension  $D$  are (Friedlander, 2000):

$$K_f(v_r, v_s) = k_0 \left( \frac{1}{v_r} + \frac{1}{v_s} \right)^{1/2} (v_r^{1/D} + v_s^{1/D}),$$

$$k_0 = \left( \frac{3}{4\pi} \right)^{\frac{2}{D}-\frac{1}{2}} \left( \frac{6k_B T}{\rho_p} \right)^{1/2} r_m^{2-\frac{6}{D}} \quad (10)$$

$$K_c(v_r, v_s) = \frac{2k_B T}{3\eta} \left( \frac{f_r}{v_r^{\frac{1}{D}}} + \frac{f_s}{v_s^{\frac{1}{D}}} \right) (v_r^{\frac{1}{D}} + v_s^{\frac{1}{D}}) \quad (11)$$

with  $v_r$  and  $v_s$  the total volume of the aggregate corresponding to same mass sphere of radius  $r$  and  $s$ , respectively, and  $f_r, f_s$  the corresponding slip correction factors. These equations reduce to those described above for spherical particles in the case of  $D = 3$ .

Cabane et al. (1993) suggested that the settling velocity of the fractal aggregates can be calculated with the same formula as for spheres, but using the fractal radius of the aggregate. Although this is a good starting point, it is important to note that the porosity of the aggregate structure allows the decrease of the drag force due to air moving through the porous structure, as verified experimentally (Johnson et al., 1996). In order to include this effect in the velocity calculations we have followed the methodology described in Tang and Raper (2002), which is based on semi-empirical models for the settling velocity of fractal aggregates. The ratio of the porosity-corrected settling velocity to the impermeable particle velocity,  $\Omega$ , can be calculated from:

$$\Omega = \frac{2\beta^2 \left( 1 - \frac{\tanh(\beta)}{\beta} \right)}{2\beta^2 + 3 \left( 1 - \frac{\tanh(\beta)}{\beta} \right)} \quad (12)$$

with  $\beta = R_f/\sqrt{\kappa}$ . Here  $\kappa$  is the permeability of the particle that is a function of the porosity  $\epsilon$ :

$$\kappa = \frac{\frac{4r_m^2}{18\psi} \left( 3 - \frac{9}{2}\psi^{1/3} + \frac{9}{2}\psi^{5/3} - 3\psi^2 \right)}{3 + 2\psi^{5/3}}, \quad \psi = 1 - \epsilon. \quad (13)$$

Finally the porosity of a fractal aggregate can be estimated based on the ratio of the fractal to monomer radius from:

$$\epsilon = 1 - \left(\frac{R_f}{r_m}\right)^{D_f-3} \quad (14)$$

Application of the above theory suggests that the correction to the particle's settling velocity is small for the size of aggregates/monomers expected in Titan's aerosols with maximum increase in the velocity of 10%. Fig. 1 presents the variation of the above parameters with the fractal radius for the case of a 50 nm monomer size.

### 2.3. Charge effects

The analysis of Titan's geometric albedo at wavelengths dominated by the haze contribution suggest an average size of aerosols smaller than 1  $\mu\text{m}$  in the stratosphere (McKay et al., 1989; Toon et al., 1992; Rannou et al., 2003; Lavvas et al., 2008b). On the other hand, microphysical models (Toon et al., 1992; Rannou et al., 2003; Lavvas et al., 2008b) predict that particles should reach a larger size before falling at the surface. Thus, an impedance to the growth of the particles was required in the simulations in order to restrain their size. This effect could be achieved with particles having the same sign charge, thus repelling each other, thereby hindering the growth due to coagulation.

Aerosols can become charged during charge exchange with ions present in the atmosphere, by electron capture, or due to photoelectron emission in the interaction with UV radiation (Bakes et al., 2002). There are three ionization regions in Titan's atmosphere that could affect the charge state of the aerosols. The main ionosphere, located at  $\sim 1100$  km and produced by high-energy photon and photoelectron deposition, the mesosphere ion layer induced by the ablation of silicate meteoroids close to 500 km, and the lower ion layer close to 70 km related with the deposition of galactic cosmic rays (GCR). A significant density of charged aerosols was observed in the thermosphere as large mass negative ions (Coates et al., 2007), proving that the particles can become charged, although the variation of this charge with altitude and time is not yet constrained by observations. Furthermore, Borucki and Whitten (2008) suggested that the photoelectric effect is insignificant for Titan's aerosols, based on the analysis of conductivity measurements from the Huygen's probe, leaving the interaction of the aerosols with ambient ions and electrons as the main process.

The inclusion of the electrostatic interaction between the particles is usually simulated with the use of a charge density parameter,  $q$ , that defines the average number of electrons per radius of a particle. Typical values of this parameter among different models range between 15 and 30 electrons per micron of particle radius

(Borucki et al., 1987; McKay et al., 1989; Toon et al., 1992; Rannou et al., 2003; Lavvas et al., 2008b). The modification factor for the coagulation rates in the case of same sign charge in the particles can be calculated from (Fuch, 1964):

$$f_e = \frac{\tau}{\exp(\tau) - 1}, \quad \tau = \frac{q^2 r s}{(r + s) k_B T} \quad (15)$$

Borucki et al. (1987) calculated the charge per radius of the aerosols using particle size distributions based on the Voyager observations and considering ionization from GCR and energetic electron precipitation from Saturn's magnetosphere. They concluded that the variation of  $q$  with altitude depended on the particle size, with constant  $q$  for small particles and decreasing  $q$  with altitude above 250 km for large particles ( $r \geq 1 \mu\text{m}$ ). Although these calculations need to be repeated based on the much more constraining Cassini/Huygens observations for the aerosol properties and the atmospheric conductivity, they show that  $q$  could vary with altitude. Nevertheless, we assume a constant  $q$  in order to simplify the calculations. The results presented below suggest that it is a valid assumption.

### 3. Application to Titan

We initiate the aerosol simulation assuming seed particles of 3 nm radius distributed in a gaussian production profile with a peak located at 1000 km and a width of 25 km. The integrated mass production rate is set to  $3.0 \times 10^{-14} \text{ g cm}^{-2} \text{ s}^{-1}$ . We choose this production altitude based on our previous analysis of the detached haze layer (Lavvas et al., 2009), which suggested that a large production of aerosols is taking place in Titan's thermosphere. The column production rate is constrained by the DISR optical properties described below, and is consistent within the range retrieved by our previous analysis. We note here that the mass flux derived at the Huygens location is not necessarily the same as the disk-average mass flux required to fit Titan's geometric albedo. This can happen if the atmospheric circulation at the aerosol production region is strong enough to affect the spatial distribution of the aerosol precursors, and also if the produced aerosols are affected by the atmospheric circulation. These issues are further discussed below.

For the particle optical properties, we use Mie theory for the spheres and the semi-empirical model of Rannou et al. (1999) for fractal aggregates. The DISR analysis used the  $T$ -matrix method (Mishchenko et al., 1996) for the aggregate optical properties. The differences between the two methods are at maximum 20% (Tomasko et al., 2008). The refractive index for the particles was initially taken from the laboratory analogs of Khare et al. (1984) and then corrected based on the DISR observations. The vertical temperature profile used in the calculations is taken from Fulchignoni et al. (2005). Atmospheric mixing is taken into account with the use of an eddy mixing profile. The sensitivity of the model results on the assumed mixing profile and the charge density is discussed below.

#### 3.1. Monomer radius

The charge present on the aerosols can constrain their maximum size due to their mutual repulsion. In the case of aggregate particles, this translates to a constraint on the number of monomers. The DISR measurements provided information for the single scattering phase function of the particles in the main haze layer, which constrains the number of monomers. Fig. 2 presents a comparison of the aerosol phase function at 100 km, for the model and the DISR observations at different wavelengths. The general behavior of the phase functions with a strongly scattering forward peak and low back-scattering is the main characteristic of the fractal

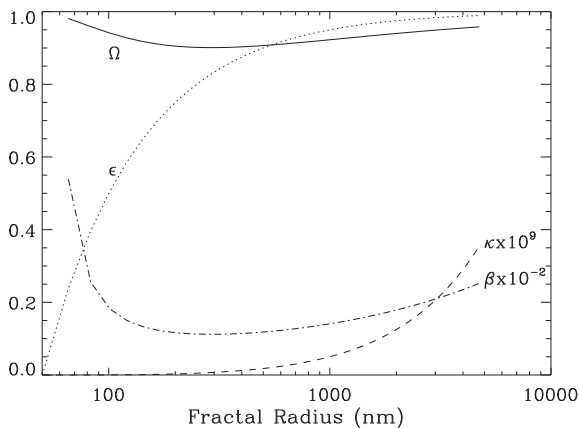
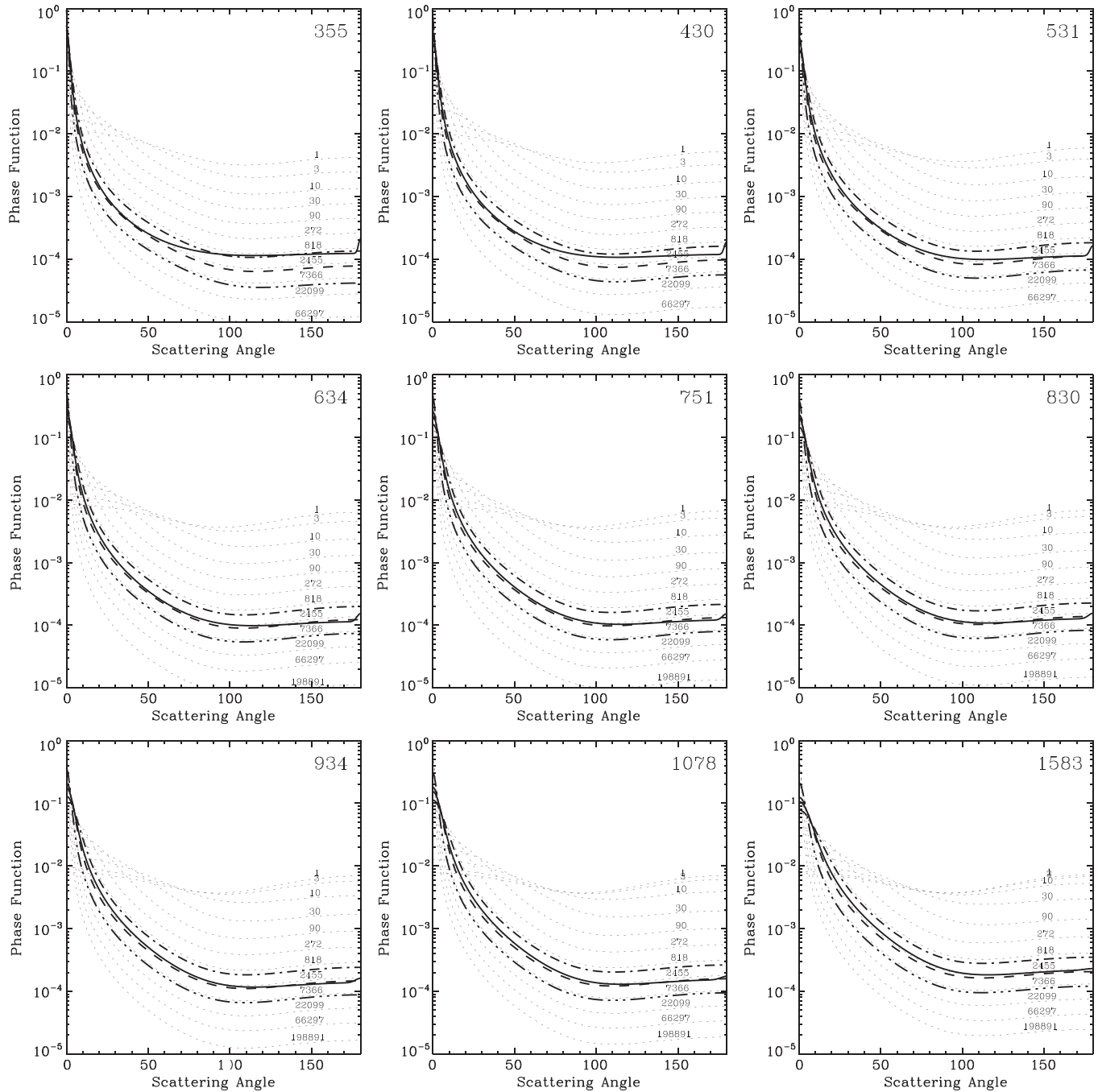


Fig. 1. Variation of porosity ( $\epsilon$ ), permeability ( $\kappa$ ),  $\beta$ , and  $\Omega$  with fractal-aggregate radius for the case of a 50 nm radius monomer. See text for details.



**Fig. 2.** Comparison between the modeled and DISR retrieved phase functions at 100 km for the given wavelength. The dotted lines correspond to the phase functions of aggregates with different number of monomers as given for each curve. The solid line corresponds to the retrieved phase function from DISR measurements (Tomasko et al., 2008) and the dashed line is the model calculated phase function for a charge density of  $15 \text{ e}/\mu\text{m}$ . The dash-dotted and dash-triple-dotted lines present the resulting phase function for 20 and  $10 \text{ e}/\mu\text{m}$ , respectively.

aggregates and a direct indication of their presence in Titan's atmosphere. The shape of the phase function depends on two parameters: the monomer radius and the number of monomers in the aggregates. There is very good agreement between the simulated and observed phase functions at all wavelengths except at 355 nm where the simulated phase function appears to have smaller values than the observed for scattering angles larger than  $90^\circ$ . Nevertheless, the calculated phase function at 355 nm is within a factor of 2 from the observed phase function, while the agreement between model and observations significantly improves at longer

wavelengths. Our calculations suggest a monomer radius of 54 nm, and the number of monomers at 100 km is  $\sim 4000$ . These values are close to the those retrieved by DISR (50 nm, 3000 monomers/aggregate), which explains the good agreement between the observed and simulated phase functions. The charge density ( $q$ ) that defines the number of monomers in the aggregates is the main parameter used to fit the model to the observations. Best agreement with the observations is achieved for  $q = 15 \text{ e}/\mu\text{m}$  with smaller and larger values providing an envelope to the measured phase functions (Fig. 2).

### 3.2. Altitude profile of extinction

The DISR extinction profiles constrain the contribution of atmospheric mixing in the aerosol density vertical profile. The extinction coefficient between 80 and 150 km has a constant scale height of 65 km. This scale height is a minimum value and could increase up to 80 km due to uncertainties in the pointing of the spacecraft at high altitudes, although there is further support for a scale height close to 65 km from ISS observations (Tomasko et al., 2008). In region I, the particle settling velocity decreases towards the surface due to the increasing contribution of atmospheric drag, thus the contribution of atmospheric mixing becomes increasingly more important. Fig. 3 presents the sensitivity of the calculated extinction to the assumed eddy profile. The extinction profiles have been normalized to the DISR results at 200 km in order to compare the slopes of the calculated extinction curves. Above ~120 km the simulated profiles are characterized by an exponential variation with a constant scale height as well. At lower altitudes though, the slope of the extinction decreases, becoming almost constant near 70 km. Below this altitude the extinction starts to increase again until the surface. This behavior is caused by the rapidly changing temperature profile in this region that changes the atmospheric density and affects the particle settling velocity, thus, the resulting aerosol opacity.

As shown in Fig. 3, the eddy mixing coefficient affects the extinction profile, with larger values providing larger scale heights. In order to constrain the magnitude of the eddy profile in region I, we consider two limiting cases. The upper limit (dotted line in Fig. 3) is retrieved by adjusting the eddy coefficient to a magnitude necessary to reproduce the observed scale height of 65 km. In this case, the calculated extinction profile is in good agreement with the observations above 120 km, but is smaller than the observed extinction profile near 80 km. For the lower limit of the eddy coefficient (dash-dotted line), we use the mixing profile derived from the distribution of gaseous species (Lavvas et al., 2008b). For this

case the calculated extinction profile is in better agreement with the observations near 80 km, but has an altitude variation characteristic of a scale height larger than 65 km. In view of these two limiting cases we chose as our nominal case, a mixing profile that provides an intermediate extinction (dashed line, Fig. 3). We should note that the constant scale height extinction profile retrieved by DISR, and followed by the abrupt transition at 80 km could be an artifact of the retrieval process and cannot preclude the more smooth behavior suggested by the analytic simulation here from being correct as well.

Tomasko et al. (2008) find that regions II and III can be characterized with constant extinction profiles. The calculations below 80 km provide an increasing extinction towards the surface for any mixing profile, in contrast to the observations. This is an indication of other processes taking place in the lower atmosphere with the most likely candidate being the condensation of gas species on the aerosol particles. This is supported by the retrieved optical properties discussed further below.

### 3.3. Size and density

The particles produced at 1000 km are assumed to have a radius of 3 nm, an estimate based on the large mass negative ions detected by Coates et al. (2007), assuming a mass density of  $1 \text{ g cm}^{-3}$ . As they settle out of the production region particles grow spherically ( $D_f = 3$ ) and their radius starts to increase (Fig. 4). At the same time the corresponding number density decreases to satisfy mass balance. Once the particles reach the transition altitude of 520 km they start to grow as fractal aggregates. The collision cross-section of aggregates is larger than the corresponding cross-section of the same volume spherical particles, hence the coagulation rates increase significantly leading to a rapid growth in the size of the particles (Fig. 4). Below 200 km where the size

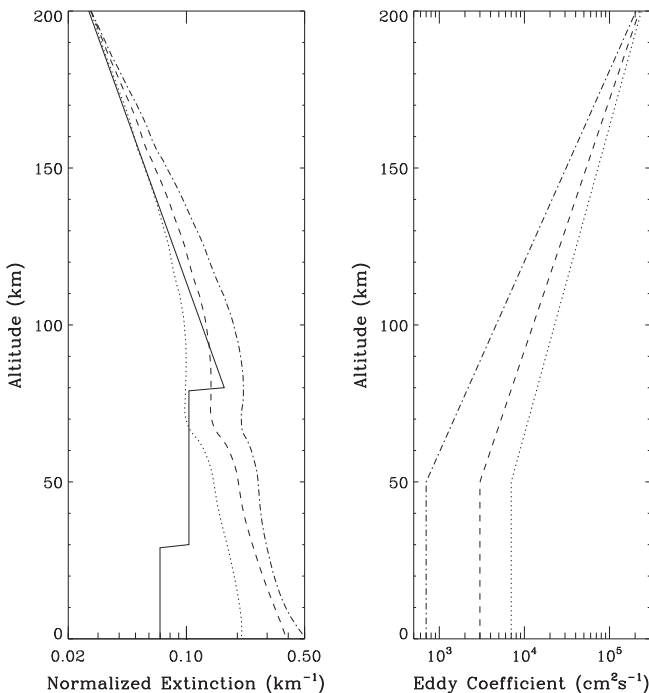


Fig. 3. Sensitivity of model results for the extinction profile on the assumed eddy mixing coefficient. Left panel presents the extinction at 355 nm, normalized to the retrieved extinction (solid line) at 200 km, for the different atmospheric mixing profiles presented on the right panel.

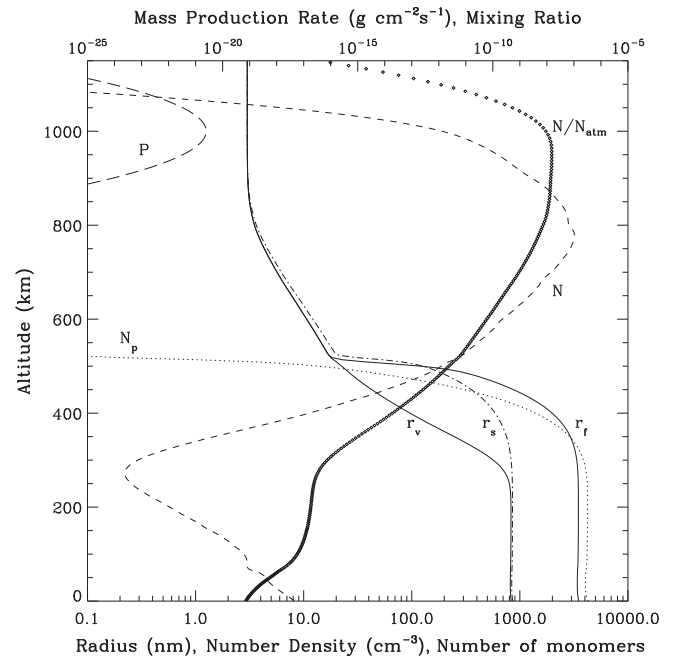


Fig. 4. Model results for the altitude variation of the particle size and density. The solid line corresponds to the volume average radius ( $r_v$ ), the dash-dotted line to the equivalent sphere surface average radius ( $r_s$ ) and the dash-triple-dotted line to the aggregate surface average radius ( $r_f$ ). The dashed line is the corresponding number density ( $N$ ) for the equivalent sphere surface average radius, the dotted line is the average number of monomers in each aggregate ( $N_p$ ) and the long-dashed line is the mass production profile ( $P$ ). The diamond symbols present the average aerosol mixing ratio (particle density/atmospheric density) corresponding to  $N$ .

distribution of the particles does not change, the volume average size of the particles is  $0.84 \mu\text{m}$  and the corresponding aggregate surface radius is  $3.4 \mu\text{m}$ . These values are close to those retrieved by Tomasko et al. (2008) in region I ( $0.72$  and  $2.03 \mu\text{m}$ , respectively). In addition, the calculated particle density at  $80 \text{ km}$  is  $3 \text{ cm}^{-3}$  in good agreement with the value of  $5 \text{ cm}^{-3}$  retrieved by Tomasko et al. (2008).

The particle size distribution is unimodal in the upper atmosphere, above the growth mode transition altitude (Fig. 5). The particles grow faster once they start to aggregate close to  $500 \text{ km}$ , which leads to a rapid loss of intermediate sizes between  $0.1$  and  $0.5 \mu\text{m}$ . Smaller particles are transported from higher altitudes, while larger particles result from the coagulation. Therefore the distribution becomes bimodal. At lower altitudes almost all particles have coagulated to sizes for which further growth is inhibited by the electrostatic repulsion due to particle charging. Hence, the particle size distribution becomes unimodal again.

### 3.4. Optical properties

For a given refractive index, the optical properties of fractal aggregates are mainly defined by the monomer radius because the opacity scales almost linearly with the number of monomers (Rannou et al., 2003). Thus, with the monomer radius constrained by the phase function, we can determine the refractive index from the single scattering albedo. This can be accomplished by calculating the scattering and absorbing properties of particles for different refractive index values and comparing the resulting single scattering albedo with the retrieved single scattering albedo from the *in situ* measurements. As discussed in Tomasko et al. (2008) the *in situ* single scattering albedo of aerosols decreases towards the near-IR, in contrast to the calculated single scattering albedo based on the Khare et al. (1984) index (Fig. 6). This difference between the retrieved and simulated single scattering albedos demonstrates that Titan's aerosols are more absorbing in the near-IR than the laboratory analogs. Based on the observed dependence of the single scattering albedo of aerosols above  $144 \text{ km}$  we have adjusted the Khare et al. (1984) imaginary part of the refractive index ( $k$ ) in order to reproduce this behavior. The resulting  $k$  variation with wavelength is presented in Fig. 7 and Table 1. For the real part of the refractive index we used the Khare et al. (1984) measurements.

The wavelength dependence of the total optical depth in the three regions is presented in Fig. 8 and compared with the model results, while Fig. 9 presents a comparison between the retrieved and modeled altitude variation of the extinction profiles and total optical depth at different wavelengths between  $355$  and  $1583 \text{ nm}$ . There is a good agreement between the retrieved and modeled

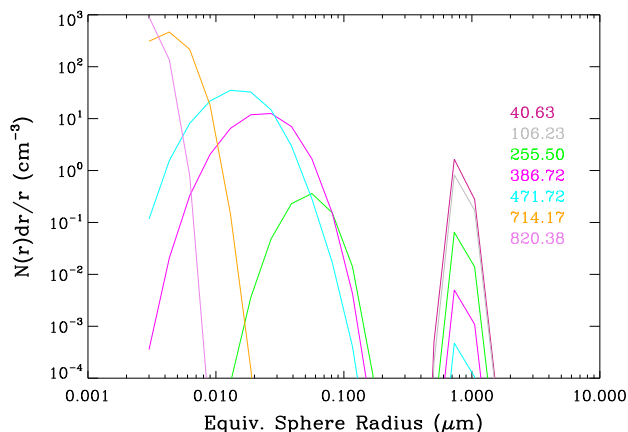


Fig. 5. Size distribution of particles at different designated altitudes, based on the model calculations.

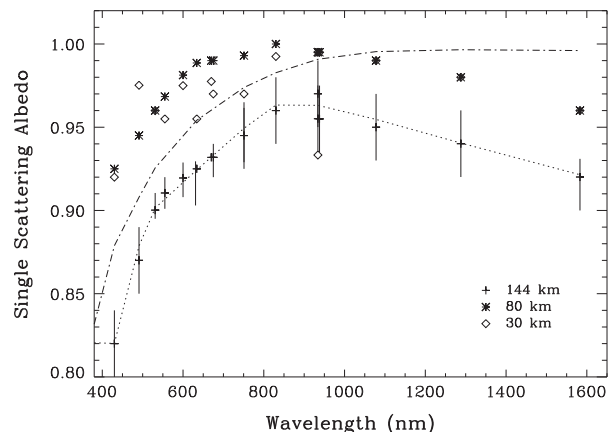


Fig. 6. Wavelength variation of single scattering albedo. The lines correspond to the model results, while the scattered data points with error bars correspond to the retrieved by DISR single scattering albedo at different altitudes. The dash-dotted line is the calculated single scattering albedo at  $144 \text{ km}$  assuming the Khare et al. (1984) refractive index, while the dotted line corresponds to the adjusted refractive index.

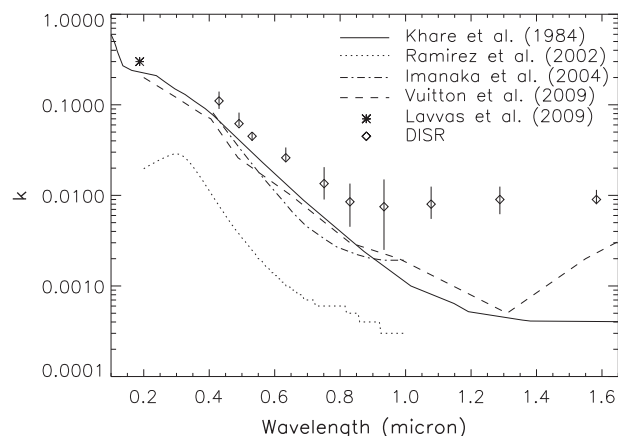


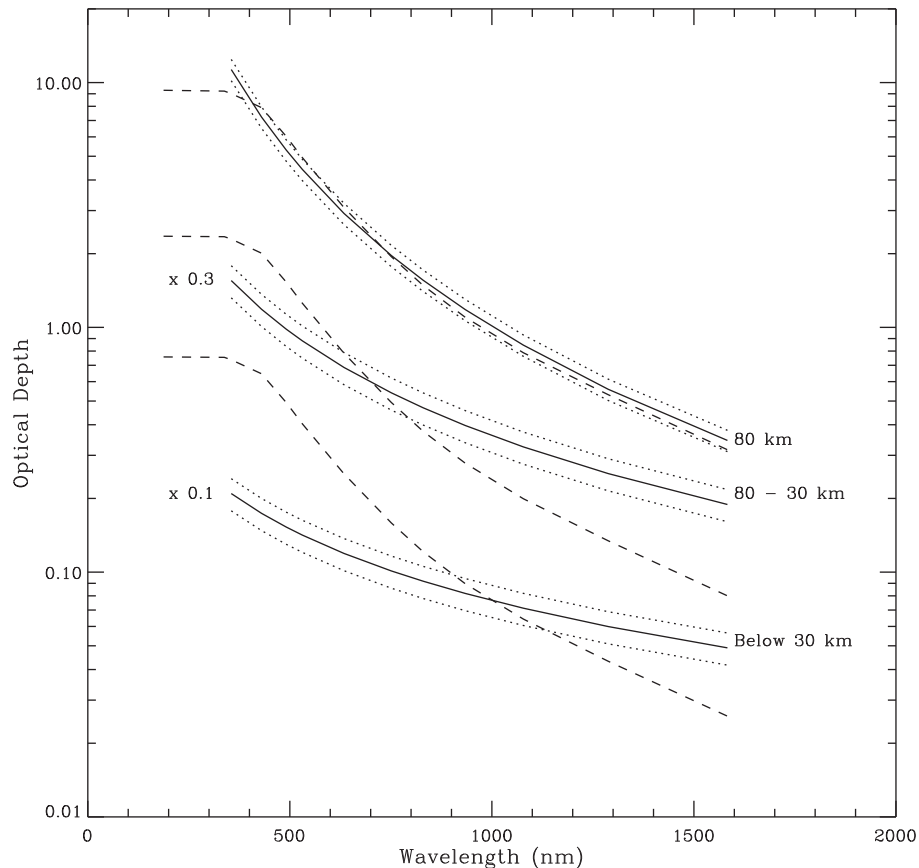
Fig. 7. Imaginary refractive indices based on different laboratory measurements (lines) along with the values for Titan's aerosols retrieved by our analysis of the DISR observations (diamonds). The error bars are based on the reported uncertainty of the retrieved single scattering albedo of the DISR measurements (Tomasko et al., 2008). The asterisk corresponds to the upper limit of the refractive index at  $187.5 \text{ nm}$  retrieved by the analysis of the detached haze layer (Lavvas et al., 2009). See above-mentioned references for further details.

Table 1

New refractive index values for Titan's aerosols based on the *in situ* DISR measurements for the single scattering albedo. The  $k$  values correspond to the points of the simulated single scattering albedo curve (dotted line) of Fig. 6 at the DISR wavelengths, while the minimum and maximum  $k$  values present the uncertainty in the retrieved index, based on the uncertainty of observed single scattering albedo. The real part of the refractive index,  $n$ , is taken from the Khare et al. (1984) measurements.

Wavelength (Å)	$n$	$k$	$k$ (min)	$k$ (max)
430	1.71	$1.10 \times 10^{-1}$	$9.00 \times 10^{-2}$	$1.40 \times 10^{-1}$
491	1.71	$6.20 \times 10^{-2}$	$5.80 \times 10^{-2}$	$8.20 \times 10^{-2}$
531	1.71	$4.50 \times 10^{-2}$	$4.00 \times 10^{-2}$	$4.90 \times 10^{-2}$
634	1.69	$2.60 \times 10^{-2}$	$2.40 \times 10^{-2}$	$3.40 \times 10^{-2}$
751	1.67	$1.35 \times 10^{-2}$	$9.00 \times 10^{-3}$	$2.05 \times 10^{-2}$
830	1.66	$8.50 \times 10^{-3}$	$4.50 \times 10^{-3}$	$1.35 \times 10^{-2}$
934	1.66	$7.50 \times 10^{-3}$	$2.50 \times 10^{-3}$	$1.50 \times 10^{-2}$
1078	1.65	$8.00 \times 10^{-3}$	$5.50 \times 10^{-3}$	$1.25 \times 10^{-2}$
1288	1.64	$9.00 \times 10^{-3}$	$6.20 \times 10^{-3}$	$1.25 \times 10^{-2}$
1583	1.64	$9.00 \times 10^{-3}$	$8.00 \times 10^{-3}$	$1.15 \times 10^{-2}$

optical properties of the particles in the altitude region above  $80 \text{ km}$  in terms of both the wavelength dependence and the magnitude of the opacity. In addition, the altitude dependence of the



**Fig. 8.** Variation with wavelength of total extinction optical depth for different altitude regions. The solid lines presents the retrieved optical depth, while the dotted lines present the uncertainty level. Dashed lines correspond to the model results for the corresponding altitude region.

extinction and total optical depth provide a good fit to the observed profiles for all wavelengths.

### 3.5. Lower altitude region

The DISR observations for the two lower altitude regions suggest that the extinction profiles are constant with altitude. At short wavelength the extinction coefficient in region II is greater than in region III, while at long wavelengths the opposite is true (Fig. 9). The simulated profiles are significantly different from this behavior and are characterized by an increasing extinction profiles towards the surface for all wavelengths. In addition, in the lower altitude regions the variation of extinction optical depth with wavelength is stronger in the model than the data, decreasing more rapidly with wavelength.

The disagreement between the model and the observations for the two lower altitude regions suggests that the aerosol properties (size and density) change relative to the properties identified in region I. Based on our calculations the microphysical processes defining the evolution of the aerosol distribution are not expected to change for altitudes below 200 km, thus, the observed variation of the retrieved optical properties is an indication of other processes taking place. Further constraints on these processes can be retrieved from the observed wavelength variation of the particle opacity.

The observed extinction coefficient at low altitudes has a much weaker wavelength dependence than predicted by the fractal aggregate model (Fig. 8). This suggests that the aerosols are more spherical in this region because the wavelength dependence of the extinction coefficient for large spherical particles is essentially

flat. Another indication of the different optical behavior of the particles below 80 km comes from the retrieved phase functions (Tomasko et al., 2008). These demonstrate an increasing back-scattering contribution towards longer wavelengths, also an indication of increasing sphericity of the particles. Finally, the retrieved single scattering albedo increases in these altitude regions relative to the values at higher altitudes (Fig. 6), which suggests that the particles are less absorbing. This can be explained by condensation of gaseous species on the aggregate particles beginning at 80 km.

On the other hand, the fact that the retrieved opacity has a behavior in between the pure aggregate structure with the strong wavelength dependence and the wavelength behavior of spherical particles suggests that the mass deposited on the particles is not enough to totally cover the aggregates and make them completely spherical (or at least erase their detailed structure). Instead the particles retain their aggregate structure but with a higher sphericity. Alternatively, the observations can be explained by a population of spherical particles along with the aggregates in these regions. Finally, the stronger wavelength dependence of the total opacity between 80 and 30 km relative to the variation between 30 km and the surface in the observations indicates that there is a larger mass increase in the particles in the latter region relative to the former. Methane has the largest mass flux available for condensation among all species in Titan's troposphere and the observed altitude variation of the total opacity correlates well with the region where methane is expected to condense. Thus, the inclusion of condensation processes in our model is necessary in order to understand the vertical structure and wavelength dependence of the DISR retrieved particle properties. A complete description of these is provided in the accompanying paper.

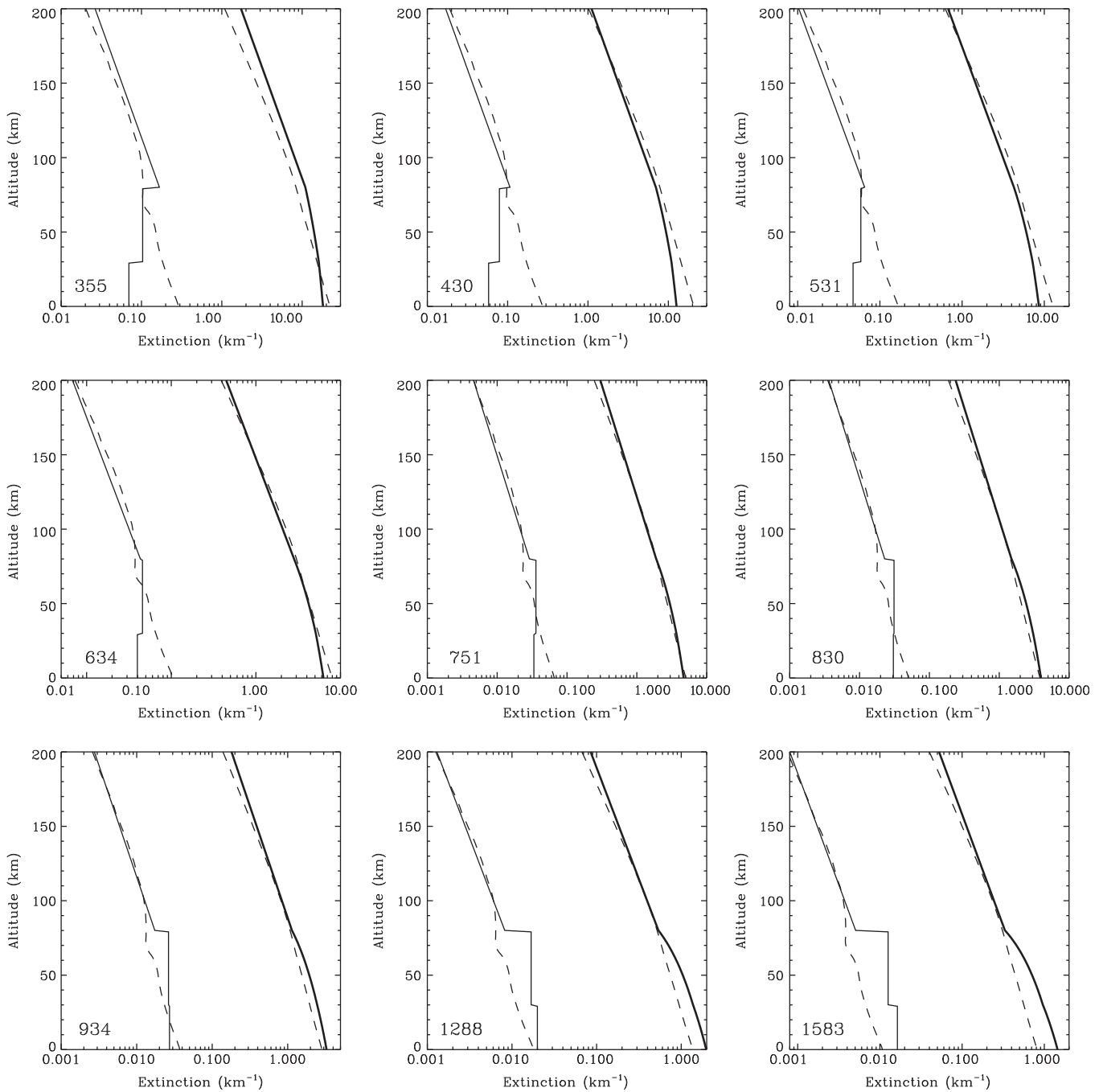


**Fig. 9.** Variation of aerosol extinction (thin lines) and total extinction optical depth (thick lines) with altitude at different wavelengths. Solid lines correspond to the DISR observations at the wavelength shown (Tomasko et al., 2008) and dashed lines to the corresponding model results (dashed line for extinction and long-dashed line for optical depth).

#### 4. Discussion

In the past, analyses of Titan's geometric albedo suggested that the tholin refractive index used in the simulations has to be multiplied by a factor of  $\sim 1.5$  in order to match the observations (McKay et al., 1989; Toon et al., 1992). This factor brings the tholin refractive index (Khare et al., 1984) very close to the retrieved index from our work between 0.43 and 0.7  $\mu\text{m}$ , but does not provide the increased absorption observed for longer wavelengths. Observations from the Cassini/VIMS instrument have also retrieved new aerosol features in the near-IR; a large absorption feature was observed at 3.4  $\mu\text{m}$  which was directly attributed to the aero-

sols, while other non-identifiable features were observed between 4.2 and 4.3  $\mu\text{m}$  (Bellucci et al., 2009). Thus, the new refractive indexes retrieved here from the DISR observations and elsewhere from other instruments should be used in any new spectroscopic investigations of aerosols in Titan's atmosphere.

The mass flux retrieved here ( $3 \times 10^{-14} \text{ g cm}^{-2} \text{ s}^{-1}$ ), is within the range  $2.7\text{--}4.6 \times 10^{-14} \text{ g cm}^{-2} \text{ s}^{-1}$ , determined by our previous analysis of the detached haze layer (Lavvas et al., 2009). Yet, in order to match the retrieved by UVIS extinction profile (Liang et al., 2007) a mass flux close to the upper boundary of this range is required. Uncertainties in the UVIS extinction profile are not well constrained since, as discussed in Liang et al. (2007), their retrieval

was a preliminary result. On the other hand, assuming that the higher production is correct, in order to match the DISR retrieved opacity in the lower atmosphere, particles must be removed from the atmosphere more efficiently. This removal is possible if the settling velocities are larger or the atmospheric mixing more effective in removing the aerosols.

Uncertainties in the settling velocity of the particles are related to the drag forces on the aggregates. Although we have attempted to correct for the non-spherical drag force on the fractal particles, these correction are based on empirical models of earth analogs, which perhaps do not hold for Titan's aerosols. Nonetheless, we expect that the possible correction to the current settling velocities should be smaller than the increase required to transport the particles faster to the surface. More likely there are other processes involved in the evolution of the aerosol distribution beyond the one dimensional description provided here.

The most likely candidate for explaining this decrease in the aerosol mass flux reaching the lower atmosphere is advection. The strong stratospheric jet observed around 300 km can transfer particles horizontally and deposit them in the polar regions where the descent section of the circulation is focused (currently at the north pole). This has been demonstrated with Titan general circulation models (Rannou et al., 2004). Advection is considered as the generating source for the detached haze layer observed by Voyager around 350 km (Rannou et al., 2002), while the same is expected for the multiple detached layers observed in the lower atmosphere in ISS images (Porco et al., 2005). Depending on the magnitude of the horizontal winds, a fraction of the particles would be able to fall through the jet region and reach the lower atmosphere and eventually the surface. The magnitude of the meridional winds at the location of the stratospheric jet is  $\sim 3 \text{ cm s}^{-1}$  (Achterberg et al., 2008), while the settling velocity of the particles is of the order of  $0.1 \text{ cm s}^{-1}$ . This suggests that over the time required to settle through one scale height (51 km at 300 km altitude) the particles can be drifted latitudinally over 1/6th of the pole to pole distance. Thus, the effective mass production rate required to match the DISR stratospheric observations could be reconciled with the aerosol production rate in the upper atmosphere required to match the UVIS extinction profile.

The DISR observations correspond to a cumulative contribution of pure aerosols and cloud particles present in Titan's lower atmosphere. Thus both particle types must eventually be considered in the calculations. Aerosols acting as nucleation sites for the condensation of gases will be covered by the condensing material, hence, they will exhibit a different interaction with the solar photons. The aerosol particle density is large enough to expect that all condensation processes will take place on their surface (heterogeneous nucleation). The main gas candidates (in terms of mass flux and altitude of condensation) involved in condensation processes in Titan's lower stratosphere and troposphere are methane, ethane and hydrogen cyanide.  $\text{C}_2\text{H}_6$  and HCN are formed in Titan's upper atmosphere from the products of  $\text{N}_2$  and  $\text{CH}_4$  photolysis, while methane's origin lies on the surface or subsurface. Due to the different source regions and thermodynamical properties, these gases can condense at different altitude regions (which can overlap), hence their impact on the observed optical properties could be large. Based on photochemical models (Yung et al., 1984; Lara et al., 1996; Lebonnois et al., 2001; Hourdin et al., 2004; Wilson and Atreya, 2004; Lavvas et al., 2008b), HCN is expected to condense close to 80 km, which correlates well with the first transition altitude detected by DISR. Ethane condensation initiates close to the tropopause, while methane condensation starts close to 8 km and extends up to the tropopause. In the accompanying paper, where we include the effects of condensation we show that the aerosol optical properties at altitudes below

80 km can be reproduced by inclusion of methane and hydrogen cyanide condensation.

## 5. Conclusions

We have used the analysis of the DISR observations (Tomasko et al., 2008) with a 1D simulation and retrieved specific information regarding the particle charge, the vertical mixing and the particle optical properties. The observations for the haze opacity in the lower atmosphere, suggest a mass production rate of aerosols of  $3 \times 10^{-14} \text{ g cm}^{-2} \text{ s}^{-1}$ , which is consistent with our previous analysis based on the optical properties of the detached haze layer at 520 km (Lavvas et al., 2009). By fitting the observed aerosol phase functions at 100 km we constrain the particle charge density to  $15 \text{ e}/\mu\text{m}$ . With this value, the microphysical model predictions for the number of monomers, and particle size and density, are in good agreement with the DISR measurements above 80 km (Tomasko et al., 2008). In addition, the aerosol optical properties demonstrate a stronger absorption index than Khare et al. (1984) with an increasing absorption toward the near-IR.

At lower altitudes, the pure aerosol simulation presented here, fails to reproduce the DISR retrieved optical properties. The particles below 80 km have an increased mass relative to the particles above but they retain their aggregate structure. Their optical properties indicate the addition of mass with different optical properties, suggesting that this happens through the condensation of gases present in Titan's lower atmosphere. These effects must be included in the calculations in order to achieve a better understanding of the processes taking place at these altitudes. The condensation in the aggregate particles is described in the accompanying paper.

## Acknowledgments

This work has been supported through NASA Grants NNX09AP14G and NNX09AB58G and NASA's Astrobiology Initiative through JPL Subcontract 1372177 to the University of Arizona.

## References

- Achterberg, R.K., Conrath, B.J., Gierasch, P.J., Flasar, F.M., Nixon, C.A., 2008. Titan's middle-atmospheric temperatures and dynamics observed by the Cassini Composite Infrared Spectrometer. *Icarus* 194, 263–277.
- Bakes, E.L.O., McKay, C.P., Bauschlicher Jr., C.W., 2002. Photoelectric charging of submicron aerosols and macromolecules in Titan's haze. *Icarus* 157, 464–475.
- Balthasar, M., Frenklach, M., 2005. Monte-Carlo simulations of soot particle coagulation and aggregation: The effect of a realistic size distribution. *Proc. Combust. Inst.* 30, 1467–1475.
- Bellucci, A., Sicardy, B., Drossart, P., Rannou, P., Nicholson, P.D., Hedman, M., Baines, K.H., Burrati, B., 2009. Titan solar occultation observed by Cassini/VIMS: Gas absorption and constraints on aerosol composition. *Icarus* 201, 198–216.
- Borucki, W.J., Whitten, R.C., 2008. Influence of high abundances of aerosols on the electrical conductivity of the Titan atmosphere. *Planet. Space Sci.* 56, 19–26.
- Borucki, W.J., Levin, Z., Whitten, R.C., Keese, R.G., Capone, L.A., Summers, A.L., Toon, O.B., Dubach, J., 1987. Predictions of the electrical conductivity and charging of the aerosols in Titan's atmosphere. *Icarus* 72, 604–622.
- Cabane, M., Chassefiere, E., Israel, G., 1992. Formation and growth of photochemical aerosols in Titan's atmosphere. *Icarus* 96, 176–189.
- Cabane, M., Rannou, P., Chassefiere, E., Israel, G., 1993. Fractal aggregates in Titan's atmosphere. *Planet. Space Sci.* 41, 257–267.
- Coates, A.J., Crary, F.J., Lewis, G.R., Young, D.T., Waite Jr., J.H., Sittler Jr., E.C., 2007. Discovery of heavy negative ions in Titan's ionosphere. *Geophys. Res. Lett.* 34, L22103.
- Friedlander, S.K., 2000. *Smoke, Dust and Haze. Fundamentals of Aerosol dynamics*, second ed. Oxford University Press. ISBN:0-19-512999-7.
- Fuch, N.A., 1964. *The Mechanics of Aerosols*. Pergamon Press, New York (translated by R.E. Daisley and M. Fuchs).
- Fulchignoni, M. et al., 2005. In situ measurements of the physical characteristics of Titan's environment. *Nature*. doi:10.1038/nature04314.
- Hourdin, F., Lebonnois, S., Luz, D., Rannou, P., 2004. Titan's stratospheric composition driven by condensation and dynamics. *J. Geophys. Res.* 109, E12005. doi:10.1029/2004JE002282.

- Imanaka, H. et al., 2004. Laboratory experiments of Titan tholin formed in cold plasma at various pressures: Implications for nitrogen-containing polycyclic aromatic compounds in Titan haze. *Icarus* 168, 344–366.
- Johnson, C.P., Li, X., Logan, B.E., 1996. Settling velocities of fractal aggregates. *Environ. Sci. Technol.* 30, 1911–1918.
- Khare, B.N., Sagan, C., Arakawa, E.T., Suits, F., Calcott, T.A., Williams, M.W., 1984. Optical constants of organic tholins produced in a simulated titanian atmosphere: From soft X-ray to microwave frequencies. *Icarus* 60, 127–137.
- Lara, L.M., Lellouch, E., Lopez-Moreno, J., Rodrigo, R., 1996. Vertical distribution of Titan's atmospheric neutral constituents. *J. Geophys. Res.* 101, 23261–23283.
- Lavvas, P.P., Coustenis, A., Vardavas, I.M., 2008a. Coupling photochemistry with haze formation in Titan's atmosphere. Part I: Model description. *Planet. Space Sci.* 56, 27–66.
- Lavvas, P.P., Coustenis, A., Vardavas, I.M., 2008b. Coupling photochemistry with haze formation in Titan's atmosphere. Part II: Results and validation with Cassini/Huygens data. *Planet. Space Sci.* 56, 67–99.
- Lavvas, P., Yelle, R.V., Vuitton, V., 2009. The detached haze layer in Titan's mesosphere. *Icarus* 201, 626–633.
- Lebonnois, S., Toubanc, D., Houdin, F., Rannou, P., 2001. Seasonal variations of Titan's atmospheric composition. *Icarus* 152, 384–406.
- Liang, M.-C., Yung, Y.L., Shemansky, D.E., 2007. Photolytically generated aerosols in the mesosphere and thermosphere of Titan. *Astrophys. J.* 61, L199–L202.
- McKay, C.P., Pollack, J.B., Courtin, R., 1989. The thermal structure of Titan's atmosphere. *Icarus* 80, 23–53.
- McKay, C.P., Pollack, J.B., Courtin, R., 1991. The greenhouse and antighenhouse effects on Titan. *Science* 253, 1118–1121.
- McKay, C.P., Coustenis, A., Samuelson, R.E., Lemmon, M.T., Lorenz, R.D., Cabane, M., Rannou, P., Drossart, P., 2001. Physical properties of the organic aerosols and clouds on Titan. *Planet. Space Sci.* 49, 79–99.
- Mishchenko, M.I., Travis, L.D., Mackowski, D.W., 1996. *J. Quant. Spectrosc. Radiat. Trans.* 55, 535–575.
- Morgan, N., Kraft, M., Balthasar, M., Wong, D., Frenklach, M., Mitchel, P., 2007. Numerical simulations of soot aggregation in premixed laminar flames. *Proc. Combust. Inst.* 31, 693–700.
- Porco, C.C. et al., 2005. Imaging of Titan from the Cassini spacecraft. *Nature* 434, 159–168.
- Pruppacher, H.R., Klett, J.D., 1978. *Microphysics of Clouds and Precipitation*. Reidel Publishing Company, Dordrecht.
- Rages, K., Pollack, J.B., Smith, P.H., 1983. Size estimate of Titan's aerosols based on Voyager high-phase-angle images. *J. Geophys. Res.* 88, 8721–8728.
- Rannou, P., Cabane, M., Chassefiere, E., Botet, R., McKay, C.P., Courtin, R., 1995. Titan's geometric albedo: Role of the fractal structure of the aerosols. *Icarus* 118, 355–372.
- Rannou, P., Cabane, M., Botet, R., Chassefiere, E., 1997. A new interpretation of scattered light measurements at Titan's limb. *J. Geophys. Res.* 102, 10997–11013.
- Rannou, P., McKay, C.P., Botet, R., Cabane, M., 1999. Semi-empirical model of absorption and scattering by isotropic fractal aggregates of spheres. *Planet. Space Sci.* 47, 385–396.
- Rannou, P., Houdin, F., McKay, C.P., 2002. A wind origin for Titan's haze structure. *Nature* 418, 853–856.
- Rannou, P., McKay, C.P., Lorenz, R.D., 2003. A model of Titan's haze of fractal aerosols constrained by multiple observations. *Planet. Space Sci.* 51, 963–976.
- Rannou, P., Houdin, F., McKay, C.P., Luz, D., 2004. A coupled dynamics microphysics model of Titan's atmosphere. *Icarus* 170, 443–462.
- Tang, P., Raper, J.A., 2002. Modelling the settling behaviour of fractal aggregates – A review. *Powder Technol.* 123, 114–125.
- Tomasko, M.G., Doose, L., Engel, S., Dafoe, L.E., West, R., Lemmon, M., Karkoschka, E., See, C., 2008. A model of Titan's aerosols based on measurements made inside the atmosphere. *Planet. Space Sci.* 56, 669–707.
- Toon, O.B., Turco, R.P., Pollack, J.B., 1980. A physical model of Titan's clouds. *Icarus* 43, 260–282.
- Toon, O.B., McKay, C.P., Griffith, C.A., Turco, R.P., 1992. A physical model of Titan's aerosols. *Icarus* 95, 24–53.
- Vuitton, V., Tran, B.N., Persans, P., Ferris, J.P., 2009. Determination of the complex refractive indices of Titan haze analogs using photothermal deflection spectroscopy. *Icarus* 203, 663–671.
- West, R.A., Smith, P.H., 1991. Evidence for aggregate particles in the atmospheres of Titan and Jupiter. *Icarus* 90, 330–333.
- West, R.A. et al., 1983. Voyager 2 photopolarimeter observations of Titan. *J. Geophys. Res.* 88, 8699–8708.
- Wilson, E.H., Atreya, S.K., 2004. Current state of modeling the photochemistry of Titan's mutually dependent atmosphere and ionosphere. *J. Geophys. Res.* 109. doi:10.1029/2003JE002181.
- Yung, Y.L., Allen, M., Pinto, J.P., 1984. Photochemistry of the atmosphere of Titan: Comparison between model and observations. *Astrophys. J. Suppl.* 55, 465–506.